PHYSICAL REVIEW C **97**, 034610 (2018)

Cluster correlation and fragment emission in ^{12}C + ^{12}C at 95 MeV/nucleon

G. Tian,[1,2] Z. Chen,[1,2,*] R. Han,[1] F. Shi,[1] F. Luo,[1] Q. Sun,[1,2] L. Song,[1,2] X. Zhang,[1,2] G. Q. Xiao,[1] R. Wada,[3,†] and A. Ono[4]
[1] *Institute of Modern Physics, Chinese Academy of Sciences, Lanzhou 730000, China*
[2] *University of Chinese Academy of Sciences, Beijing, 100049, China*
[3] *Cyclotron Institute, Texas A&M University, College Station, Texas 77843, USA*
[4] *Department of Physics, Tohoku University, Sendai 980-8578, Japan*

(Received 12 January 2018; published 19 March 2018)

The impact of cluster correlations has been studied in the intermediate mass fragment (IMF) emission in ^{12}C + ^{12}C at 95 MeV/nucleon, using antisymmetrized molecular dynamics (AMD) model simulations. In AMD, the cluster correlation is introduced as a process to form light clusters with $A \leqslant 4$ in the final states of a collision induced by the nucleon-nucleon residual interaction. Correlations between light clusters are also considered to form light nuclei with $A \leqslant 9$. This version of AMD, combined with GEMINI to calculate the decay of primary fragments, reproduces the experimental energy spectra of IMFs well overall with reasonable reproduction of light charged particles when we carefully analyze the excitation energies of primary fragments produced by AMD and their secondary decays. The results indicate that the cluster correlation plays a crucial role for producing fragments at relatively low excitation energies in the intermediate-energy heavy-ion collisions.

DOI: 10.1103/PhysRevC.97.034610

I. INTRODUCTION

In the intermediate-energy heavy-ion collisions from a few tens MeV/nucleon to several hundred MeV/nucleon, a variety of reaction phenomena and mechanisms are realized depending on the sizes of the projectile and the target nuclei, the incident energy, and the impact parameter. Generally, it is expected that the composite system composed of projectile and target nuclei in violent central collisions is compressed and excited in the early stage of the reactions, and then the hot and dense nuclear system expands and breaks up through a multifragmentation process so that the whole system disintegrates into many light particles with the atomic number $Z \leqslant 2$ and intermediate mass fragments (IMFs) with $Z \geqslant 3$. As two of the basic experimental observables, the energy spectra and angular distributions of the emitted particles are influenced by the nuclear mean field and nuclear dynamics of collisions and play key roles for studying the transport mechanism of nucleons in nuclear systems. Furthermore, a detailed study on nuclear reaction dynamics can provide valuable information of nuclear matter properties, such as equation of state, liquid-gas phase transition, and many-body correlations.

The ^{12}C + ^{12}C reaction at 95 MeV/nucleon was performed at GANIL motivated by the hadron beam therapy with carbon ions to treat cancerous tumors, and the experimental data are available in Ref. [1–3]. In our previous work in Ref. [4], we studied the emission mechanism of the light charged particles (LCPs) and IMFs, using an improved antisymmetrized molecular dynamics (AMD) code, called AMDV-FM [5]. The AMDV-FM reproduces the experimental data fairly well in their global characteristics, but in detail the yields of the projectilelike component of all LCPs are slightly overpredicted and IMF yields at $\theta_{\rm lab} > 20^\circ$ are poorly reproduced for most of the isotopes by a factor of $2 - 10$. In this paper we would like to present a further improvement of the transport simulation, especially focusing on the IMF production mechanisms.

In order to elucidate the reaction dynamics, many microscopic transport models for nuclear collisions have been developed. In these transport models the time evolution of one-body distribution function of the many-nucleon system is treated. Most of the current nuclear reaction transport models either rely on the mean-field models, such as Boltzmann-Uehling-Uhlenbeck (BUU) equation, or on molecular dynamics models, such as quantum molecular dynamics (QMD), which were supposed to be suitable for describing the fragmentation process in heavy-ion collisions because of consideration of many-nucleon correlations at least in the sense of classical dynamics. In AMD approach [6], the full antisymmetrization of many-nucleon wave function was taken into account, which is an important quantum feature. The versions in Refs. [7,8] were also an important extension to understand the fragment formation and the single-particle dynamics by introducing quantum fluctuation for the emergence of many fragmentation channels. However, it should be noted that these versions were introduced mainly to consider the single-nucleon motion in the mean field, not directly the many-body correlations, particularly the cluster correlations to form light nuclei (such as deuterons and α particles).

The production of clusters in transport models is very important. Unfortunately, most transport models cannot describe clusters properly due to the assumption of single-nucleon motion in the mean field. In order to predict the cluster productions, a lot of efforts have been made. In Ref. [9], for example, the coalescence approaches have been applied to the results

---

[*] zqchen@impcas.ac.cn
[†] wada@comp.tamu.edu

of transport calculations assuming that the correlations do not affect the time evolution of the single-nucleon distribution. Another important work was done by Danielewicz *et al.* [20]. In their extended version of BUU approach (pBUU), the cluster up to ^{3}H and ^{3}He were introduced and treated as the new species, though the α particles were not incorporated in this extended model. A recent calculation of this specific model demonstrates that the collision dynamics is influenced by the clusters [10]. In the AMD approach, cluster correlations have been introduced by improving the two-nucleon collision process [11–13]. The aims of this paper are to report the present status of this approach and to demonstrate the importance of a proper treatment of clusters in the studies of heavy-ion collisions.

This paper is organized as follows. In Sec. II, the version of AMD used in the present work is briefly described. In Sec. III, detailed comparisons between the experimental data and the AMD model simulations are presented. In Sec. IV, IMF emission mechanisms are further studied, using events. A brief summary is given in Sec. V.

II. ANTISYMMETRIZED MOLECULAR DYNAMICS MODELS

A. Basic part of AMD

In AMD, the wave function of an A-nucleon system $|\Phi\rangle$ is described by a Slater determinant,

$$|\Phi\rangle = \frac{1}{\sqrt{A!}}\det[\varphi_i(j)], \tag{1}$$

where

$$\varphi_i = \phi_{Z_i}\chi_{\alpha_i}. \tag{2}$$

The label α_i represents the spin and isospin of the ith single particle state, $\alpha_i = p\uparrow, p\downarrow, n\uparrow$, or $n\downarrow$, and χ is the spin and isospin wave function. The spatial wave function ϕ_{Z_i} is represented by a Gaussian wave function,

$$\langle \boldsymbol{r}|\phi_{Z_i}\rangle = \left(\frac{2\nu}{\pi}\right)^{3/4}\exp\left[-\nu\left(\boldsymbol{r}-\frac{\boldsymbol{Z}_i}{\sqrt{\nu}}\right)^2+\frac{1}{2}\boldsymbol{Z}_i^2\right], \tag{3}$$

where $\nu = 0.16$ fm^{-2} is a parameter, which corresponds to the width of the wave packet, and the complex variables $Z \equiv \{\boldsymbol{Z}_i; i = 1,\dots,N\} = \{Z_{i\sigma}; i = 1,\dots,N, \sigma = x,y,z\}$ represent the centroids of the wave packets. If we define real vectors $\boldsymbol{D}$ and $\boldsymbol{K}$ as

$$\boldsymbol{Z} = \sqrt{\nu}\boldsymbol{D} + \frac{i}{2\hbar\sqrt{\nu}}\boldsymbol{K}, \tag{4}$$

then they correspond to the position and momentum centroids of the wave packet,

$$\frac{\langle\phi_Z|\boldsymbol{r}|\phi_Z\rangle}{\langle\phi_Z|\phi_Z\rangle} = \boldsymbol{D},\ \frac{\langle\phi_Z|\boldsymbol{p}|\phi_Z\rangle}{\langle\phi_Z|\phi_Z\rangle} = \boldsymbol{K}. \tag{5}$$

However, $\boldsymbol{D}_i$ and $\boldsymbol{K}_i$ cannot always be interpreted as physical positions and momenta of nucleons due to the effect of antisymmetrization. Equation (1) is very simple, but it is sufficient to describe the ground state of nuclei. For example, the binding energies obtained by the frictional cooling method [14] coincide with the experimental data within the precision of 1 MeV/nucleon [15]. Therefore we can expect that the initial state of the reaction and the individual channel wave functions in the intermediate and final states are well described by the AMD wave functions.

The time evolution of the wave packet centroids Z may be determined by the time-dependent variational principle,

$$\delta\int dt\frac{\langle\Phi(Z)|(i\hbar\frac{d}{dt}-H)|\Phi(Z)\rangle}{\langle\Phi(Z)|\Phi(Z)\rangle} = 0, \tag{6}$$

from which the equation of motion for Z is obtained,

$$i\hbar\sum_{j\tau}C_{i\sigma,j\tau}\frac{dZ_{j\tau}}{dt} = \frac{\partial\mathcal{H}}{\partial Z_{i\sigma}^*}. \tag{7}$$

A Hermitian matrix $C_{i\sigma,j\tau}$ with $\sigma,\tau = x,y,z$ is defined by

$$C_{i\sigma,j\tau} = \frac{\partial^2}{\partial Z_{i\sigma}^*\partial Z_{j\tau}}\log\langle\Phi(Z)|\Phi(Z)\rangle, \tag{8}$$

and $\mathcal{H}$ is the expectation value of Hamiltonian after the subtraction of the spurious kinetic energy of the zero-point oscillation of the center of masses of fragments [6,16]

$$\mathcal{H}(Z) = \frac{\langle\Phi(Z)|H|\Phi(Z)\rangle}{\langle\Phi(Z)|\Phi(Z)\rangle} - \frac{3\hbar^2\nu}{2M}A + T_0[A - N_F(Z)], \tag{9}$$

where $N_F(Z)$ is the fragment number and T_0 is $3\hbar^2\nu/2M$ in principle but treated as a free parameter for the adjustment of the binding energies of nuclei. The quantum Hamiltonian

$$H = \sum_{i=1}^{A}\frac{\boldsymbol{p}_i^2}{2M} + \sum_{i<j}v_{ij} \tag{10}$$

includes an effective two-body interaction. In this paper all calculations are performed, using the SLy4 force [17].

As mentioned, due to the effect of antisymmetrization, the centroids of Gaussian wave packets $\{\boldsymbol{Z}\}$ do not always have the meaning as the positions and momenta of nucleons. For example, in the ground state of ^{12}C, all $\boldsymbol{Z}$ are almost at the same point, but this does not mean that all nucleons are at the same point in the phase space. This is not convenient in introducing two-nucleon collisions in a way similar to usual transport models. So the coordinates $\boldsymbol{Z}$ are transformed to a new coordinates $\{\boldsymbol{W}\} = \{\boldsymbol{W}_i; i = 1,\cdots,A\}$, which can be interpreted as the centroids of incoherent wave packets. The real parts $\boldsymbol{R}_i$ and the imaginary parts $\boldsymbol{P}_i$ of $\boldsymbol{W}_i$

$$\boldsymbol{W}_i = \sqrt{\nu}\boldsymbol{R}_i + \frac{i}{2\hbar\sqrt{\nu}}\boldsymbol{P}_i \tag{11}$$

can be treated as physical positions and momenta of nucleons in the two-nucleon collision processes. Considering a few requirements, which should be satisfied by physical coordinates $\boldsymbol{W}_i$ [18], they are defined as

$$\boldsymbol{W}_i = \sum_{j=1}^{A}(\sqrt{Q})_{ij}\boldsymbol{Z}_j, \tag{12}$$

with

$$Q_{ij} = \frac{\partial}{\partial(\mathbf{Z}_i^* \cdot \mathbf{Z}_j)} \ln\langle\Phi(\mathbf{Z})|\Phi(\mathbf{Z})\rangle. \tag{13}$$

The two-nucleon collision process with Pauli blocking was formulated by using these physical coordinates [6].

B. Cluster correlations in AMD

This extended version of AMD is developed mainly to improve the description of the IMF emission by taking into account the cluster correlation. A two-nucleon collision process in AMD is a transition from an initial state $|\Psi_i\rangle$ to one of possible final states $|\Psi_f\rangle$, which is assumed to occur instantaneously and conserve the energy expectation value $\langle\Psi_i|H|\Psi_i\rangle = \langle\Psi_f|H|\Psi_f\rangle$. As the transition is induced by the residual interaction V between the two colliding nucleons, the transition rate may be expressed as

$$W_{i\to f} = \frac{2\pi}{\hbar}|\langle\Psi_f|V|\Psi_i\rangle|^2\delta(E_f - E_i). \tag{14}$$

However, some care should be taken since the transition is considered here between states that are not eigenstates of an unperturbed Hamiltonian. So an important question here is how to choose the complete basis $|\Psi_f\rangle$ of the final states. If the correlations exist in the final states between the scattered nucleons and other nucleons, it is reasonable to construct the final states by taking into account these correlations.

Cluster correlations can exist in nuclear medium under some conditions [19,20]. We assume here that clusters with $A = 2$, 3, and 4 can propagate in the medium if it is allowed by the Pauli principle. In AMD, if several wave packets (with different spins or isospins) are placed at the same phase-space point, these wave packets will tend to move together as a cluster by the equation of motion. On the other hand, if the wave packets are placed randomly in the phase space, the chance for these nucleons to form a cluster after propagation is small, i.e., the classical bound phase space does not correspond to the weight for a bound quantum state. Therefore, in order to respect the possibility of forming a cluster, the set of final states $|\Psi_f\rangle$ should be suitably constructed.

For the procedure of the transition to clusterized states, we employ the same method and the same set of parameters as those of Ref. [12]. As an example of possible final state $|\Psi_f\rangle$ for a collision of two nucleons N_1 and N_2 with the initial relative velocity v_{NN}, let us consider a process that $N_1(N_2)$ forms a cluster $C_1(C_2)$ with another particle $B_1(B_2)$ in the final state,

$$N_1 + B_1 + N_2 + B_2 \to C_1 + C_2. \tag{15}$$

This process includes the collisions without cluster formation as the special case of $C_j = N_j$ $(j = 1,2)$ with empty B_j. The partial differential cross section to this final channel is given by

$$\begin{aligned} &v_{NN}d\sigma(N_1B_1N_2B_2 \to C_1C_2)\\ &= \frac{2\pi}{\hbar}|\langle\varphi_1'|\varphi_1^{\mathbf{q}}\rangle|^2|\langle\varphi_2'|\varphi_2^{-\mathbf{q}}\rangle|^2|M|^2\delta(E_f - E_i)\frac{p_{\mathrm{rel}}^2dp_{\mathrm{rel}}d\Omega}{(2\pi\hbar)^3}, \end{aligned} \tag{16}$$

where M is the matrix element for the two-nucleon scattering to the final state with the relative momentum p_{rel} and the scattering solid angle Ω in the two-nucleon center-of-mass system. The overlap matrix $\langle\varphi_1'|\varphi_1^{+\mathbf{q}}\rangle$ is taken between $|\varphi_1^{+\mathbf{q}}\rangle = e^{i\mathbf{q}\cdot\mathbf{r}}|\varphi_1\rangle$ and $|\varphi_1'\rangle$, where $|\varphi_1\rangle$ and $|\varphi_1'\rangle$ are the initial and final states of the $N_1 + B_1$ system, respectively, and the operator $e^{i\mathbf{q}\cdot\mathbf{r}}$ gives the momentum transfer to nucleon N_1. The clusterized states $|\varphi_1'\rangle$ and $|\varphi_2'\rangle$ are approximated by the simple harmonic oscillator $(0s)^n$ configuration with the oscillator constant associated with the wave packet width ν in AMD, so that any final states of the collision is represented by an AMD wave function.

The actual situation of a two-nucleon collision requires more consideration because there are many possible ways of forming a cluster for each N of the scattered nucleons N_1 and N_2. For a scattered nucleon N, we first consider the possibility that N may form a cluster with one of the nucleons $\{B_k; k = 1,2,\ldots\}$, which have the same spin-isospin state. The cluster-formed state is denoted by $|\Phi_k'\rangle$, which is obtained by first changing the state to $|\Phi^{\mathbf{q}}\rangle$ by the momentum transfer $\mathbf{q}$ to N, and then moving the two wave packets of N and B_k to the same phase-space point without changing their center of mass. Since the different final states are not orthogonal $\mathcal{N}_{kl} = \langle\Phi_k'|\Phi_l'\rangle \neq \delta_{kl}$, the probability that N forms a cluster with one of $\{B_k\}$ should be calculated as

$$P = \sum_{kl}\langle\Phi^{\mathbf{q}}|\Phi_k'\rangle\mathcal{N}_{kl}^{-1}\langle\Phi_l'|\Phi^{\mathbf{q}}\rangle = \sum_k|v_k|^2, \tag{17}$$

$$v_k = \sum_l\mathcal{N}_{kl}^{-1/2}\langle\Phi_l'|\Phi^{\mathbf{q}}\rangle. \tag{18}$$

With this probability P, a cluster will be formed with one of $\{B_k\}$. It is somewhat arbitrary which one of $\{B_k\}$ should be chosen with what probability. This partial probability should replace the overlap probability $|\langle\varphi_1'|\varphi_1^{\mathbf{q}}\rangle|^2$ or $|\langle\varphi_2'|\varphi_2^{\mathbf{q}}\rangle|^2$ in Eq. (16). With the rest probability $(1 - P)$, the particle N does not form a cluster with a nucleon of this spin-isospin state. The procedure is repeated for other spin-isospin states for B. The particle N in the above description should be regarded as a cluster, instead of a scattered nucleon, if a (sub)cluster has been already formed in previous steps of the repetition. It should be noted that the probability factors for different contributions of the formed clusters (C_1,C_2) described in this way are functions of the relative momentum p_{rel} (or the momentum transfer $\mathbf{q}$) and the value of p_{rel} that conserves the energy depends on (C_1,C_2).

Even when the cluster formation is introduced, the many-body state is always represented by an AMD wave function, which is a Slater determinant of nucleon wave packets. The time evolution of the many-body state is solved just as usual without depending on whether some of the wave packets form clusters due to collisions in the past (except for the cluster-cluster binding process explained below). This is in contrast to the case of pBUU by Danielewicz *et al.* [14] where clusters are treated as new particle species. In our approach, a cluster may be broken by the mean field or by a two-nucleon collision between a nucleon in it and another nucleon in the system such as a process $d + X \to n + p + X'$. It is also possible that, in the final state of this two-nucleon collision, the same cluster is formed again such as an elastic process $d + X \to d + X'$. Thus various kinds of cluster reactions are taken into account without introducing many parameters. We only need to assume some in-medium two-nucleon cross sections (or matrix elements). We use free cross sections in this paper.

Many of light nuclei (Li, Be, etc.) have only one or a few bound states, which may be regarded as bound states of internal clusters. The quantum-mechanical probability of forming such a nucleus is not consistent with the semiclassical phase space with which it can be formed in the standard treatment of AMD. Therefore, for a better description, the intercluster correlation should be introduced as a stochastic process of binding clusters.

The basic procedure in the actual calculation is to replace the relative momentum between clusters by zero if moderately separated clusters ($1 < R_{\text{rel}} < 5$ fm) are moving away from each other with a small relative kinetic energy ($\mathbf{R}_{\text{rel}} \cdot \mathbf{V}_{\text{rel}} > 0$ and $\frac{1}{2}\mu V_{\text{rel}}^2 < 12$ MeV where μ is the reduced mass). The method is similar to Ref. [12] but with a different set of parameters. In addition to these conditions, linking is allowed only if each of the two clusters is one of the four closest clusters of the other when the distance is measured by $[(\mathbf{R}_{\text{rel}}/3\ \text{fm})^2 + (\mathbf{V}_{\text{rel}}/0.25c)^2]^{1/2}$. It is further required one (or both) of the two clusters is an α cluster or is in a light nucleus already bound at a previous time. Two clusters in different already-bound light nuclei are not linked. Nonclustered nucleons are treated here in the same way as clusters but two nucleons are not allowed to be linked directly. Two clusters also should not be linked directly if they can form an α or lighter cluster due to the combination of their spins and isospins. It is possible that more than two clusters are eventually linked by these conditions. However, the process is canceled unless the mass of the linked system is in the range $6 \leqslant A \leqslant 9$, and therefore the binding usually occurs in dilute environment. The binding is performed for the linked system by eliminating the momenta of clusters in the center-of-mass frame of the linked system. Energy conservation should be achieved by scaling the relative radial momentum between the center of mass of the linked system and a third cluster, which we choose to be the cluster that has the minimum value of

$$(r + 7.5\ \text{fm})(1.2 - \cos\theta)/\min(\epsilon_{\parallel},5\ \text{MeV}), \tag{19}$$

where r and $\epsilon_{\parallel}$ are the distance and the radial component of the kinetic energy for the relative motion between the linked system and the third cluster. The factor with the angle θ between the relative coordinate $\boldsymbol{r}$ and the momentum $\boldsymbol{p}$ is introduced to favor the case of $\boldsymbol{r} \parallel \boldsymbol{p}$. If the selected third cluster is already in a bound light nucleus, the light nucleus is used as the third cluster for the energy conservation.

The present AMD version has introduced cluster correlations based on the original AMD version [6] and does not take into account the wave packet branching process, such as diffusion or shrinking process [7,21]. It is an important future problem how to improve cluster correlations and single-particle motions consistently, though it is empirically known that the introduction of cluster correlations and that of the wave packet branching can similarly improve fragment production.

III. RESULTS

In this section comparisons between the simulated results and the experimental data are presented. All simulated events have been treated for the secondary decay process, using GEMINI++ [22]. Similar to the previous works, in the following discussion we use the name of the different source components, projectilelike (PLF), targetlike (TLF), and intermediate velocity (IV) sources, which are defined in a three moving source analysis in the previous work [4], to evaluate the quality of the simulated results. See details in Ref. [4].

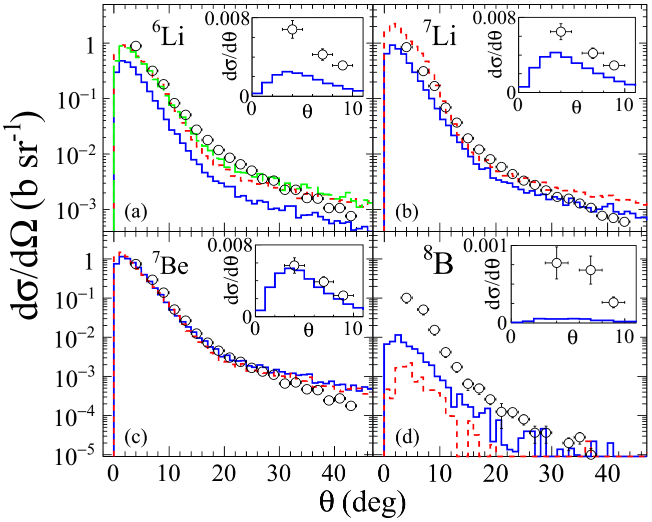

FIG. 1. Comparisons of angular distributions of $A = 6$–8 isotopes with impact parameter ranges $b = 0$–8 fm in (a)–(d), respectively. The experimental data from Ref. [1] are shown by open circles. Inserts are the same data in $d\sigma/d\theta$, but given in a linear scale in an expanded angular range of 0°–11°. The calculated results of AMD+GEMINI are shown by blue solid lines. Red dashed curves are those when IMFs with $E_x > E_{\text{pth}}$ are forced to decay. See details in Sec. IV C. For the green long-dashed histogram for ^{6}Li see also discussion in Sec. IV C.

A. IMF

1. Angular distribution and energy spectra for $A = 6$–*8*

Here the comparisons of angular distribution and energy spectra of IMFs with $6 \leqslant A \leqslant 8$ are performed between the simulated results and the experimental data. The experimental data are inclusive. The calculation is performed in the impact parameter range of $b = 0$–8 fm and the comparisons are made in an absolute scale. In Fig. 1, the results of angular distributions are shown. The experimental angular distributions (open circles) of ^{7}Li and ^{7}Be are rather well reproduced by the simulation (thick blue lines). Those with the forced decay (red dashed lines) are discussed in Sec. IV. On the other hand, the production of ^{6}Li and ^{8}B are significantly underestimated, including the PLF component shown in a linear scale in the inserts. In Fig. 2, the comparisons of energy spectra are presented. The simulation reproduces the general features of the PLF and IV source at most of angles. However, the PLF component of ^{8}B is very weak. We will discuss possible reasons for the significant underpredictions for ^{6}Li and ^{8}B in Secs. IV C and IV D.

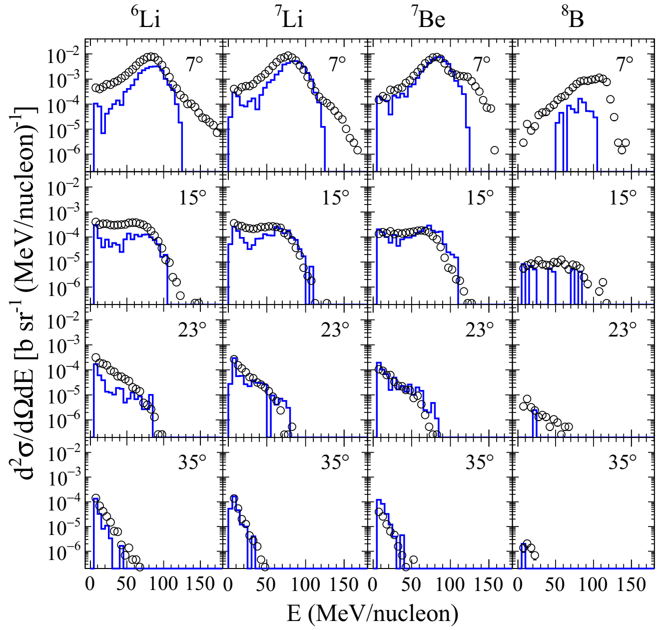

FIG. 2. Comparisons of energy spectra of $A = 6$–8 isotopes at selected angles. The experimental data are shown by open circles. The calculated results of AMD+GEMINI are shown by blue solid lines.

2. *Angular distribution and energy spectra for* $A = 9$–12

In this section, similar comparisons are presented but for heavier IMFs with $9 \leqslant A \leqslant 12$. For these fragments, Fig. 3 shows their angular distributions. As shown in the inserts the PLF components are well reproduced for relatively heavy isotopes (^{10}B, ^{11}B, ^{11}C, ^{12}C) at 4°–9°. For ^{9}Be, the calculation overpredicts the yields. For ^{10}C and ^{10}Be, it underpredicts significantly. As seen at large angles, the IV components are significantly overpredicted for all of these isotopes. In Fig. 4, the energy spectra for these isotopes are shown. As one can see at $\theta = 7^\circ$, the spectral shape of the PLF component is well reproduced for IMFs with $Z = 4$ and 5, but for carbon isotopes, the calculated widths are slightly wider. This may be caused by the large contribution of the IV component in the lower-energy side in the simulation. For all these isotopes, the IV component at large angles are overpredicted by more than a factor of 5. More detailed discussions for these model predictions will be made in Sec. IV.

B. LCP

We compare the results for LCPs here. In Fig. 5, the angular distributions are shown. The calculated results are shown for the primary AMD products (green dotted) and the final AMD+GEMINI products (blue solid) [those with the forced-decay (red dashed) are discussed in Sec. IV]. It is generally seen that the shape of the angular distributions are rather well reproduced by the simulation (blue histograms). For the proton yield, however, the AMD+GEMINI calculation underestimates the experimental cross sections by a factor of ∼2 at all angles. A similar trend is observed for deuterons. On the other hand, for α particles, AMD+GEMINI reproduces the experimental data well in the entire angular range. The reproduction of tritons is between those of deuterons and α particles, but ^{3}He, which is the mirror nucleus, is poorer at the forward angles. Except for ^{3}He, significant yields at forward angles are contributed by the feeding of the secondary decay products from the excited IMFs. For ^{3}He, on the other hand, the feeding contribution is very small at all angles. Figure 6 shows the energy spectra of LCPs. In the proton spectra, the high-energy tail ($E \gtrsim 100$ MeV) is well reproduced at all the angles. We see that the underprediction of the proton yield seen in Fig. 5 is due to the underprediction at low energies. The spectra for ^{3}He and ^{4}He are also reproduced reasonably well by the calculation except for the underpredictions of the low-energy part. The experimental data of these spectra at $\theta = 7^\circ$ show extended high-energy tails, but they are not seen at 4° and 9°, which are not shown here, and therefore these may be caused by the energy calibration at high-energy side at this angle [4]. The calculated energy spectra of tritons are quite similar to those of ^{3}He, except for the peak height in the $\theta = 7^\circ$ spectrum corresponding to the difference between tritons and ^{3}He already seen in the angular distributions in Fig. 5. On the other hand, the experimental data shows discontinuity of the triton spectra at a certain energy, which is not reproduced by the calculation. A similar disagreement is also seen in the deuteron spectra.

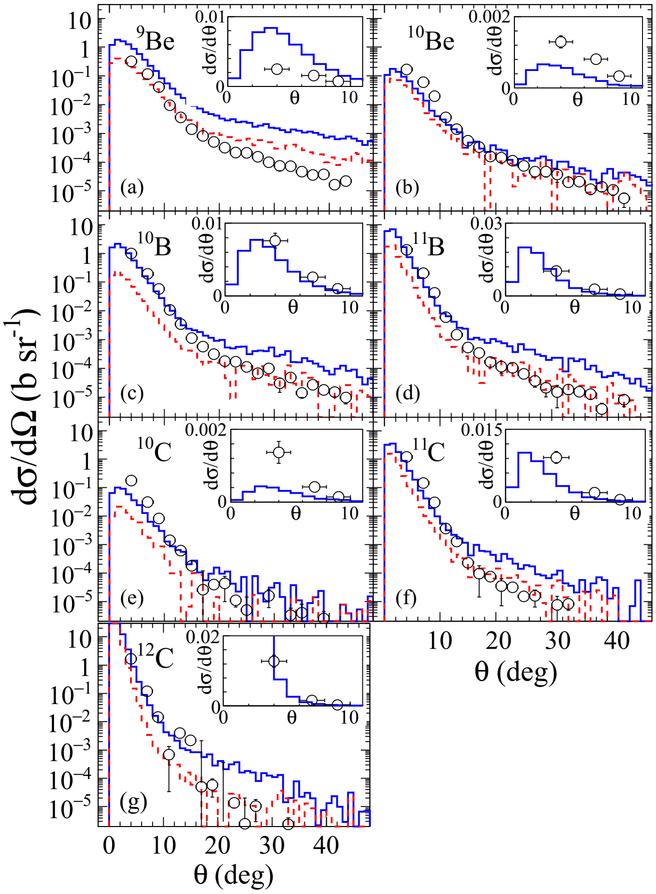

FIG. 3. Comparisons of angular distributions of $A = 9$–12 isotopes in (a)–(g), respectively. See also Fig. 1 caption.

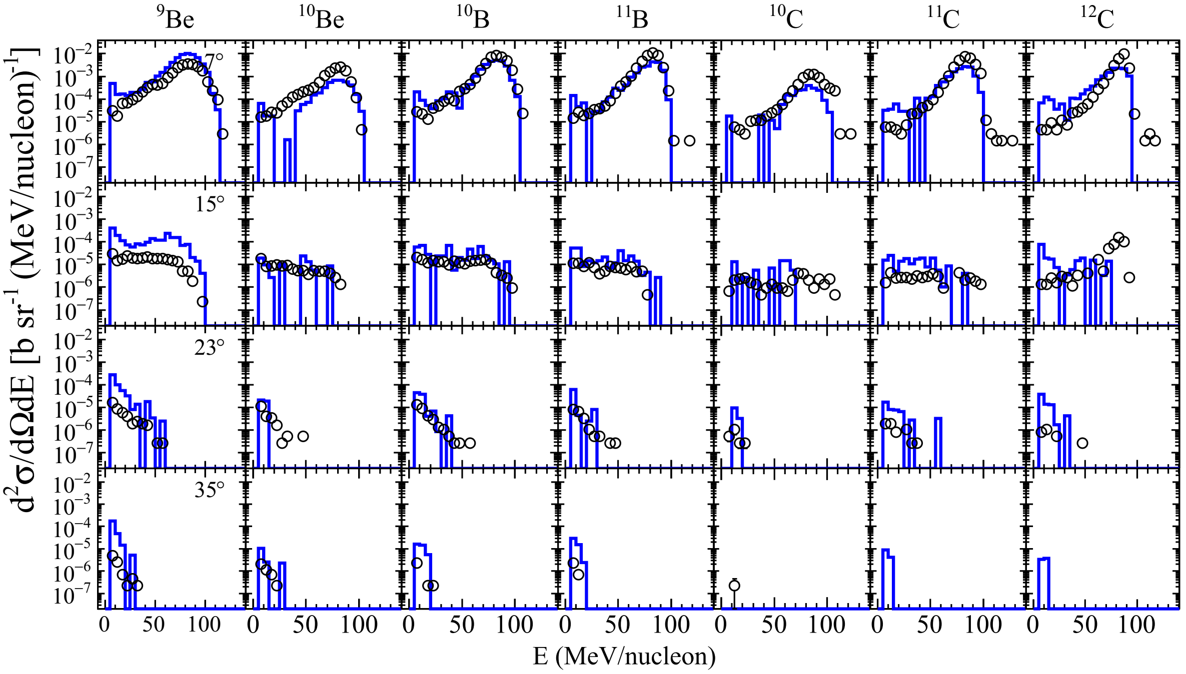

FIG. 4. Comparisons of energy spectra of $A = 9$–12 isotopes. Symbols and lines are same as those in Fig. 2.

C. Cross section

In order to see the reproduction of the yields of isotopes systematically, angle-integrated cross sections are shown in Fig. 7, where the integration is performed over all measured angles from 4°–43° in Fig. 7(a) and over 20°–43° in Fig. 7(b). As one can see, the AMD+GEMINI calculation reproduces the cross sections rather well for most particles measured except for some specific nuclei. As we have already seen in the angular distributions and energy spectra, the yield of ^{9}Be is overestimated and the yields of ^{8}B, ^{6}Li, ^{10}Be, and ^{10}C are underestimated. When one focuses on the IV component emission as shown in Fig. 7(b), one can see even better agreement for LCPs and IMF with $A < 8$ between the experimental data and the simulations, but distinct differences in heavier IMFs ($A > 8$) for which the calculation overpredicts the yields by a factor of more than 5. In the following section, we discuss these discrepancies related to the IMF emission mechanism and sequential decay process.

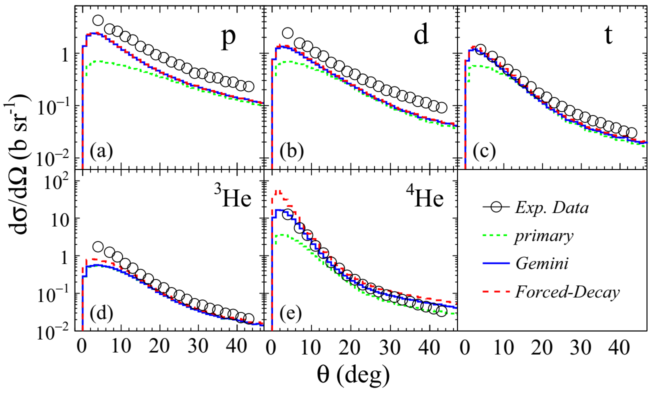

FIG. 5. Comparisons of angular distributions of light charged particles for p,d,t, ^{3}He, and ^{4}He in (a)–(e), respectively. Blue solid histograms are from the final products of AMD+GEMINI, the green dotted ones are from the primary products of AMD, and the red dashed ones are from the final products with the forced-decay which is discussed in Sec. IV.

IV. IMF PRODUCTION MECHANISM

In this section IMF emission mechanisms are investigated, using the events generated by AMD with the afterburner GEMINI++ unless otherwise specified.

A. Impact parameter distributions

In Fig. 8, the impact parameter distributions are presented for IMFs emitted at $\theta_{\text{lab}} > 20^\circ$ without and with the experimental energy threshold [1], which are typically ~5–8 MeV/nucleon. When the experimental energy thresholds are not taken into account (red histogram), the yields of these IMFs show bell shape distributions in a logarithmic plot except for those with $A = 12$ in Fig. 8(d). However, when the experimental energy thresholds are applied (blue dashed histogram), the yield of each isotope decreases significantly. The shape of the distributions becomes similar for all cases and the yield decreases rapidly as the mass increases. The significant difference between with and without the energy thresholds indicates that the majority of the large IMFs emitted at $\theta_{\text{lab}} > 20^\circ$ originate from the target residues, which have very small kinetic energy in the laboratory frame. However, one should note that when the energy thresholds are taken into account, still notable amount of IMFs are emitted at

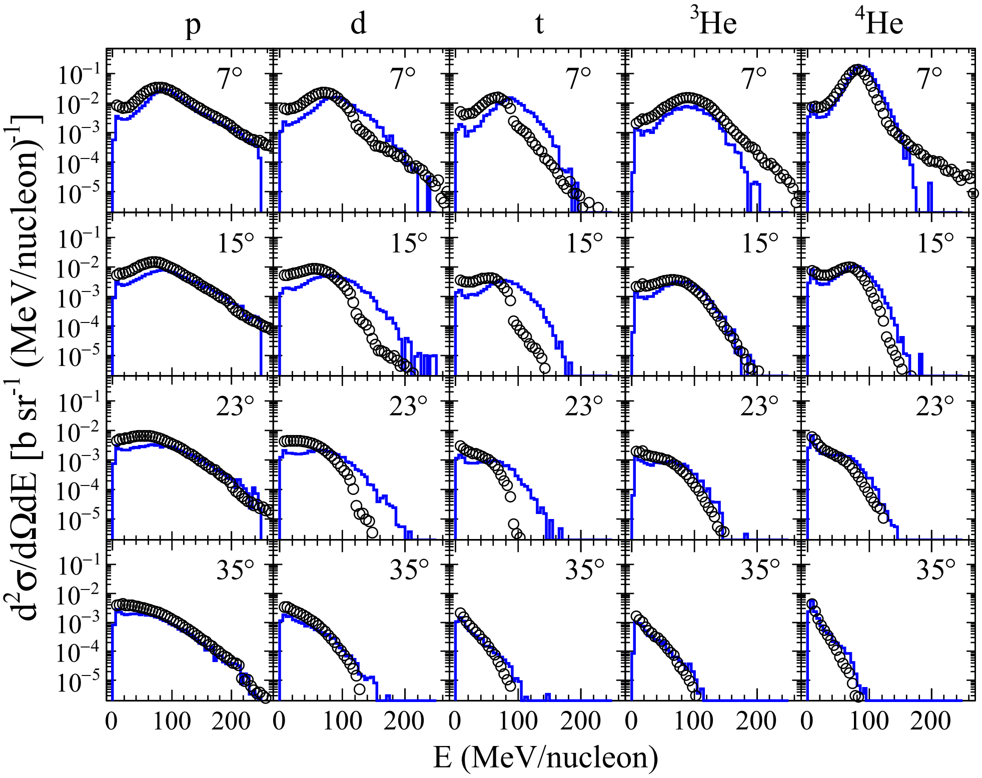

FIG. 6. Comparisons of energy spectra of light charged particles at selected angles. Symbols and lines are same as those in Fig. 2.

$\theta_{\mathrm{lab}} > 20^\circ$ in the simulation and their yields become maximum at the central collisions. The energy distributions of these IMFs are shown in Figs. 2 and 4, which indicates that these originate from the IV source component. The similarity of the impact parameter distributions for all IMFs with the energy threshold (blue dashed histograms) suggests that they originate from a similar emission mechanism. In order to shed light on the emission mechanism for these IMFs in the model, further investigations have been performed below.

B. Density distributions

In Fig. 9, the time evolutions of density distributions are plotted for two events with an emission of ^{6}Li in Figs. 9(a) and 9(b) and ^{12}C in Figs. 9(c) and 9(d), respectively, for central collisions ($b = 2.0$ fm and $b = 0.2$ fm, respectively).

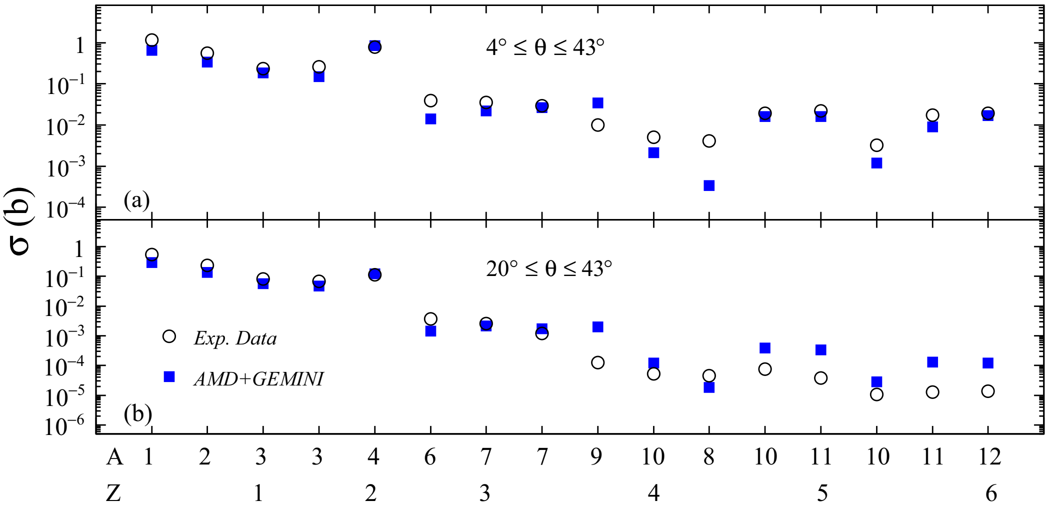

FIG. 7. Comparisons of angle-integrated cross sections over the different measured angular ranges between the AMD+GEMINI calculations and the experimental data are shown for (a) all experimentally observed over 4°–43° and (b) those over 20°–43°. The experimental data are shown by open circles. The calculated results of AMD+GEMINI are shown by blue solid squares.

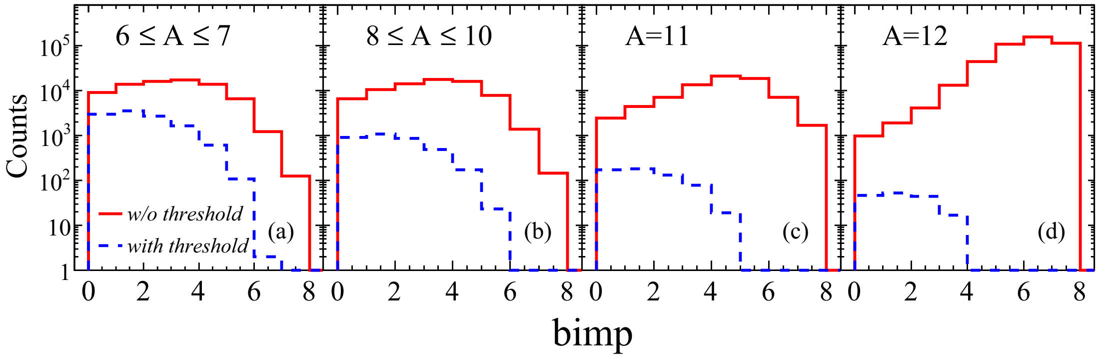

FIG. 8. Impact parameter distributions of various isotopes calculated with the AMD model for IMFs emitted at $\theta_{\mathrm{lab}} > 20^\circ$ with different masses of the primary fragments. In top of each figures (a)–(d), they are indicated. Red solid and blue based histograms represent the calculated results without and with taking into account the experimental energy threshold, respectively.

In Figs. 9(a) and 9(c) for each event, the whole nucleons from the projectile and the target are plotted. In Figs. 9(c) and 9(d), on the other hand, only projectile nucleons are shown. The impact parameter shift is taken on the X axis in the AMD simulation. In each case, only one ^{6}Li or ^{12}C is emitted at $\theta_{\mathrm{lab}} > 20^\circ$ with the energy above the detection energy threshold. In the plotted events, ^{6}Li is emitted at $\theta_{\mathrm{lab}} = 42^\circ$ and $E_{\mathrm{lab}} = 13.3$ MeV/nucleon with the excitation energy $E_{\mathrm{x}}/A = 1.4$ MeV, and ^{12}C at $\theta_{\mathrm{lab}} = 28^\circ$ and $E_{\mathrm{lab}} = 9.9$ MeV/nucleon with $E_{\mathrm{x}}/A = 1.9$ MeV. The projectile and the target are fully overlapped around $t \sim 30$ fm/c and then the system starts to expand and undergoes multifragmentation, but keeping a forward-backward binary emission pattern as seen in the right two columns of each event. This indicates that most particles, especially IMFs, emitted at the forward hemisphere in the center of mass system, originate from the projectile nucleons even though the collision is almost a central collision, suggesting that the nuclear semitransparency plays an important role in the multifragmentation process in this incident energy regime [23–25]. In fact, 4 of 6 nucleons in ^{6}Li are from the projectile and 9 of 12 nucleons in ^{12}C are from the target in these events. The semitransparency is also observed in the original AMD calculation [24]. In order to verify the semitransparency mechanisms, a momentum distribution and a phase-space (P_z, Z) distribution as a function of time are plotted in Fig. 10 for the same ^{12}C event in Fig. 9(c). When two nuclei, the projectile and the target, pass through each other ($t \sim 50$ fm/c), the P_x-P_z distribution on the left column

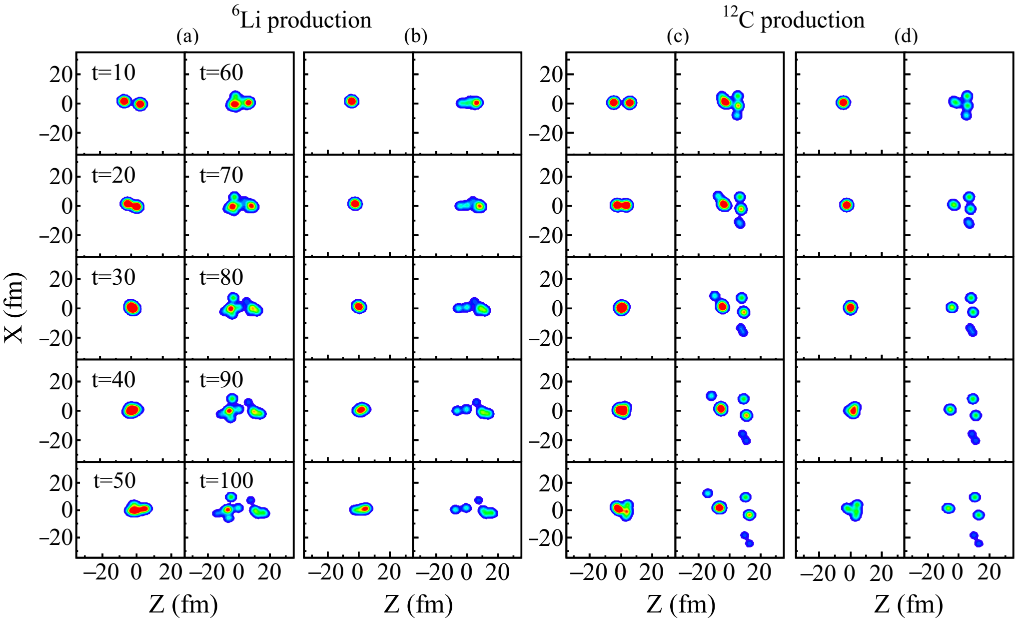

FIG. 9. Time evolution of nuclear density distributions in the center of mass system, projected on the reaction plane (X-Z plane, Z being the beam direction), for calculated events for central collisions. Reaction time is indicated in unit of fm/c in each panel of the left two columns. The smallest circle indicates a nucleon. See details in the text.

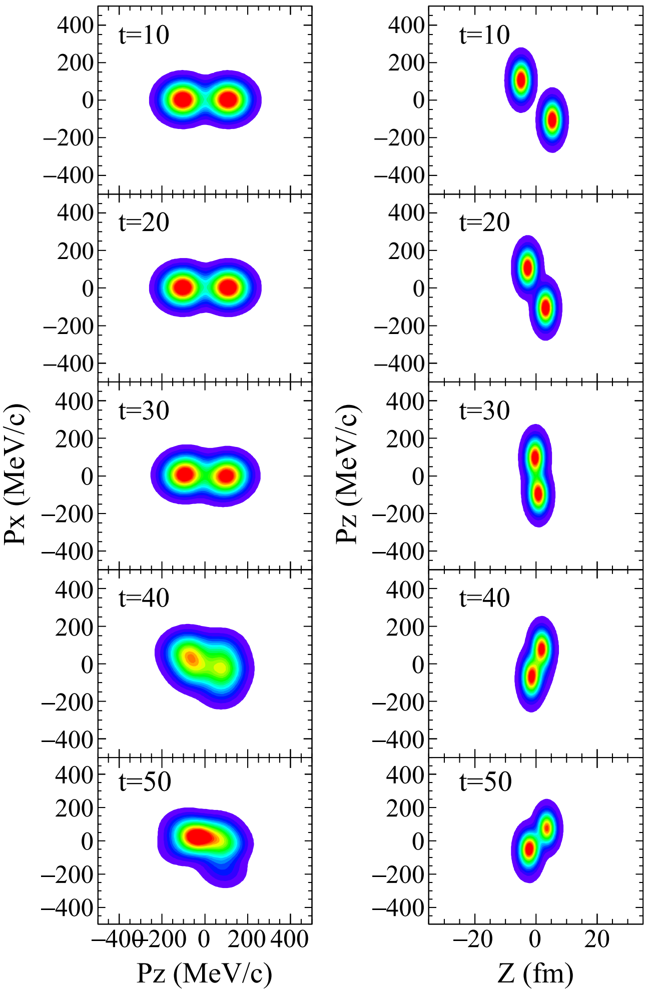

FIG. 10. (Left) Time evolution of the momentum distribution projected in the X-Z plane for the same ^{12}C event in Fig. 10. (Right) Time evolution of the phase space distribution projected in the P_z-Z plane for the same ^{12}C event in Fig. 10.

indicates a significant energy dumping in the beam direction. On the other hand, on the right, one can clearly observe that P_z of the projectile (or target nucleons) keeps moving toward the beam direction (toward the opposite direction to the beam) on average, even though the collision is near central ($b \sim 0.2$ fm). Most of the projectile nucleons pass through the target and appear on the opposite side with keeping the same direction of the momentum. This is consistent to the experimental observation in intermediate heavy-ion collisions [23–25]. For ^{6}Li emission, both projectile and target are multifragmented after passing through each other. For ^{12}C case, one remains as a large fragment. Apparently these large fragments are expected to be excited because of the energy dumping as seen in the P_x-P_z distribution on the left column, but survived for the deexcitation process by GEMINI. We will further examine the secondary process below.

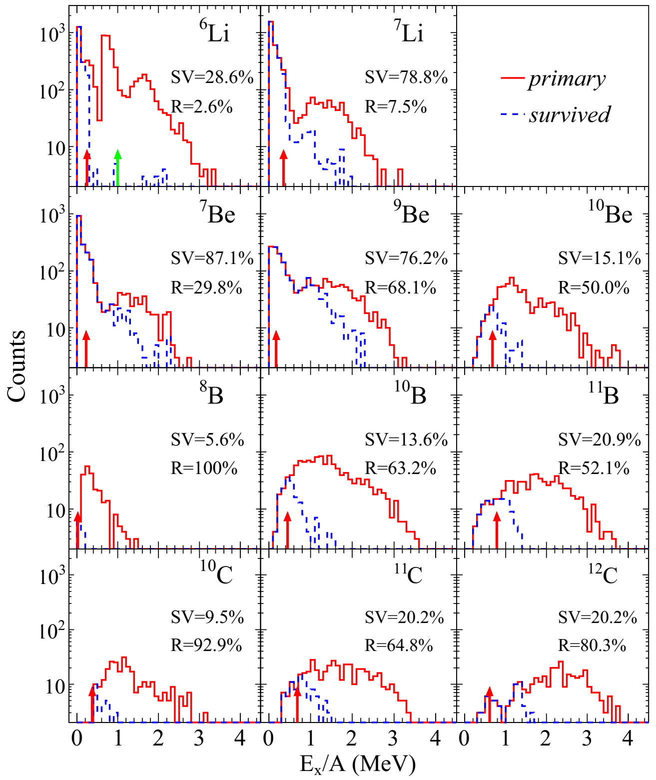

FIG. 11. Excitation energy distributions of each fragment emitted at $\theta_{\text{lab}} > 20^\circ$ and with kinetic energies above experimental energy thresholds. Red solid and blue dashed histograms represent those for the excited primary and survived secondary fragments, respectively. The particle decay thresholds are also shown on the X axis by red arrows. The green arrow in the ^{6}Li plot, see in the text. For SV and R values, see also in the text.

C. Secondary decay effect

In order to calculate the excitation energies of the primary fragments, the binding energy table of ground-state nuclei in a wide range of isotopes with $Z \leqslant 24$ are calculated separately using AMD with the SLy4 interaction [17] and stored in the binding energy table. When the primary fragments are defined on event-by-event basis using a coalescence technique with a coalescence radius of 5 fm at the end of the AMD calculation ($t = 300$ fm/c), we have the information of the internal wave function $|\Phi_{\text{frag}}\rangle$ for each fragment. Following the usual prescription, the excitation energy E_x is evaluated by subtracting the binding energy from the internal energy $\langle\Phi_{\text{frag}}|H|\Phi_{\text{frag}}\rangle$, which is the expectation value of the Hamiltonian with the subtraction of the center-of-mass kinetic energy in a way similar to Eq. (9). In Fig. 11 we show the excitation energy distributions of fragments observed at $\theta_{\text{lab}} > 20^\circ$, i.e., the IV component, and with kinetic energies above the detection energy thresholds. (The same energy threshold is applied also for the primary fragments.) The red histograms show the distributions of the excitation energies E_x of the primary fragments produced by AMD. An interesting observation is that many primary light IMFs with $A \leqslant 9$ are produced in AMD with very low excitation energies peaked near $E_x = 0$ even though these fragments in the IV component have been

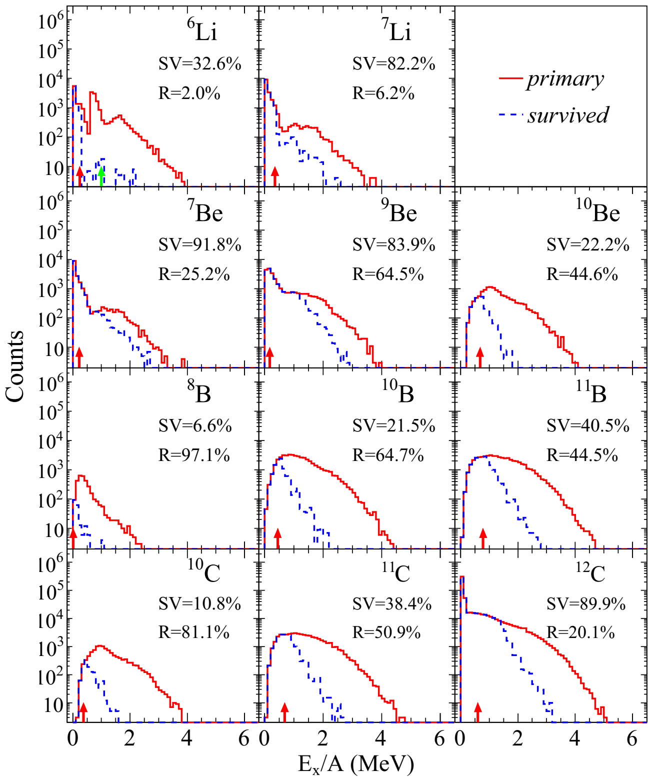

FIG. 12. Similar plots to Fig. 11, but at $\theta_{\mathrm{lab}} < 20^\circ$.

emitted from violent collisions. This is in coincidence with the method for the intercluster correlations introduced in the present version of AMD to form light nuclei with $6 \leqslant A \leqslant 9$. In most isotopes, there is another broad component centered around $E_x/A \sim 2$ MeV. The blue histograms represent the distributions of the primary excitation energies E_x for the survived fragments, which did not decay by GEMINI. In each plot, the survivability of the primary nucleus, SV, is given as the ratio of the number of the survived fragments to the total number of the primary fragments for each isotope, that is, the ratio of blue dashed histogram to that of red solid histogram. IMFs with $A \leqslant 9$ show a rather high survivability due to the sharp low-energy peak, except for ^{6}Li and ^{8}B. On the other hand, for the survived nuclei, the ratio, R, is defined as the ratio between yields with $E_x > E_{\mathrm{pth}}$ and the whole, where E_{pth} is the particle decay energy threshold.

Figure 12 shows the excitation energy distributions for the fragments emitted to forward angles $\theta_{\mathrm{lab}} < 20^\circ$ in a similar way to Fig. 11. The sharp peaks near $E_x = 0$ are seen again for light nuclei with $A \leqslant 9$ in coincidence with the method for the intercluster correlations. For heavy primary fragments such as $A = 11$, the position of the broad peak is shifted to the low-energy side ($E_x/A \lesssim 1$ MeV) compared with the case for $\theta_{\mathrm{lab}} > 20^\circ$, which suggests that some PLFs are only gently excited by the removal of nucleon(s) from the projectile. The ^{12}C nuclei also have a large component in low excitation energies. However, the lowest bin of the excitation energy includes the projectile nuclei, which did not interact with the target.

As one can see in these figures, many primary fragments with $E_x > E_{\mathrm{pth}}$, indicated by those above red arrows in the figures, remain as final products after applying GEMINI. It might be caused by the very large neutron and proton separation energies for a reduced particle decay width in the GEMINI code, but it is not certain how reasonable it is, because none of the known low-lying states above the α-particle threshold have any significant γ strength [26]. In order to see the effect of possible decays of some of these final IMFs, the survived fragments with $E_x > E_{\mathrm{pth}}$ are forced to decay by a particle emission. The emission channels are calculated with the decay probability assumed to be proportional to $e^{-E_{\mathrm{pth}}/T}$, where $T = \sqrt{E_x/A \times 8\ \mathrm{MeV}}$, without Coulomb energy, spins, and angular momentum. The results are shown by red dotted histograms in Figs. 1, 3, and 5 for IMFs and LCPs. For LCPs, the noticeable forced-decay contribution is only observed for α particles, which originate from a large cross section of peripheral collisions (6 fm $< b <$ 8 fm). In these collisions most of the survived ^{12}C nuclei with $E_x > E_{\mathrm{pth}}$ are forced to decay into 3 α. The final yields overpredict the yields below $\theta < 10^\circ$ and above $\theta > 30^\circ$. The former is closely relate to the excited PLF and the latter to the excited TLF. The latter yield is very sensitive to the detector threshold. On the other hand, a significant reduction is observed for the IMF yields with $A > 8$. The reproduction of angular distributions for the IV component of these IMFs are significantly improved and the yields become consistent with the experimental yields for most of cases. On the other hand their PLF yields are underpredicted notably for most of cases. For ^{6}Li and ^{7}Li, the red dashed histograms become above the blue solid ones at $\theta < 10^\circ$ and large angles. This is caused by the feeding from the particle decay of larger IMFs, discussed in the next subsection.

There are two nuclei for which yields are significantly underpredicted, ^{6}Li and ^{8}B. Here we discuss for ^{6}Li while ^{8}B is to be discussed in the next section. As one can see in the excitation energy distribution for ^{6}Li in the top left of Figs. 11 and 12, there are two peaks below 1 MeV/nucleon. This is caused by the different spin configurations in the low-energy states for ^{6}Li, the energies of which are calculated in AMD as

$$\begin{aligned}
&(1212)\ \mathrm{B.E.} \sim -34\ \mathrm{MeV}\\
&(2121)\ \mathrm{B.E.} \sim -34\ \mathrm{MeV}\\
&(1221)\ \mathrm{B.E.} \sim -30\ \mathrm{MeV}\\
&(2112)\ \mathrm{B.E.} \sim -30\ \mathrm{MeV},
\end{aligned} \tag{20}$$

where the notation ($Z_\uparrow\ Z_\downarrow\ N_\uparrow\ N_\downarrow$) indicates the spin-isospin configuration. In the case of (1212) for example, there is one proton with spin up, two protons with spin down, one neutron with spin up, and two neutrons with spin down. The states (1212) and (2121) corresponds to the $M = -1$ and $M = 1$ states of the actual ground state of ^{6}Li with $J^\pi = 1^+$. On the other hand, the $M = 0$ state is a superposition of (1221) and (2112), but AMD does not use the superposition of Slater determinants, and each of (1221) and (2112) has an energy expectation value higher than the ground-state energy due to the mixture of excited states. When the spin-isospin configuration is one of two upper configurations in the final ^{6}Li, their excitation energy distribution corresponds to the lowest

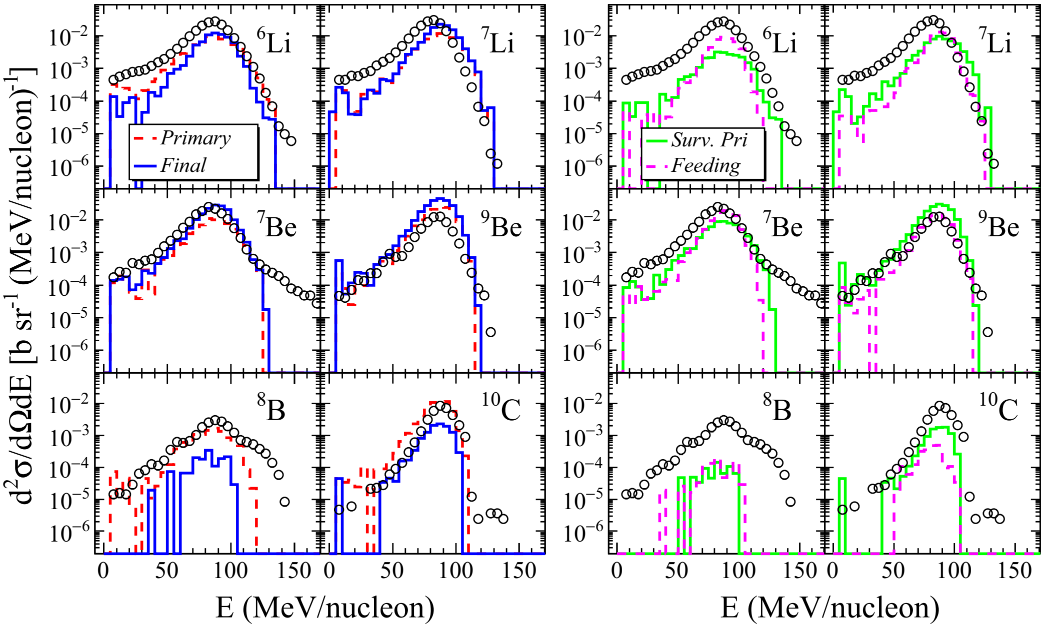

FIG. 13. (Left) Energy spectra of the experimental data and the calculated results at 4° for the primary fragments (red dashed histograms) and final secondary products (blue solid histograms). (Right) Similar plots to the left, but with calculated results for the survived primary fragments (green solid histograms) and feeding from large parents (magenta dashed histograms). The experimental data are shown by open circles.

peak (∼0 MeV) in the top left of Figs. 11 and 12. When the ^{6}Li is one of the lower two configurations, their excitation energies start from ∼4 MeV corresponding to the peak near $E_x/A \sim 0.7$ MeV. Therefore when the particle decay threshold is set to the experimental energy threshold, most of ^{6}Li in this second peak decay through a particle decay channel, but half of them should not actually decay. When we set the particle decay threshold above the second peak as show by the green arrow, ^{6}Li at both peaks remains as the survived primary and the result is shown by the green dashed histogram in the upper left of Fig. 1. The reproduction of ^{6}Li yield is improved significantly and becomes comparable to that of ^{7}Li case.

D. PLF production

A large part of PLF component is produced in excited states as shown in Fig. 12, and therefore their particle decay process affects significantly the final PLF yield. In order to shed light on the missing PLF component in the final ^{8}B spectra in the AMD+GEMINI simulation, in Fig. 13 energy spectra of several isotopes at the most forward angle (4°) are compared between the experimental data (circles) and the calculated results. On the left, red dashed histograms are those of the primary fragments and blue solid histograms are the final products after the secondary decay by GEMINI. In this section no forced decay is applied for the IMFs with $E_x > E_{\mathrm{pth}}$. For ^{8}B the primary fragment yields are as much as the observed yields, but the final yields after the secondary decay process are about a factor of 10 times smaller. For other isotopes the primary and final yields are more or less comparable. These final products are the sum of the survived primary fragments and the feeding contribution from heavier parents through particle decays. In order to see the two different contributions to the final yields, on the right side of the figure, the survived primary contribution (green solid) and the feeding contribution (magenta dashed) are plotted separately. For ^{7}Li, both processes have more or less equally contributed to the final yields. In general the energy distribution of the feeding contribution has narrower width because the width of the PLF component of the parents is narrower as the parent mass increases. For ^{6}Li and ^{7}Be, the feeding contributions are dominated. On the other hand for ^{10}C, the survived primary contribution dominates the final yields. For ^{9}Be, two thirds of the final yields originates from the survived primary fragments. Therefore, the feeding yields depend on the availability of the possible heavier parent isotopes and their decay properties. For ^{8}B, both contributions are comparable, but they are ∼10 times smaller than the observed yields distributions.

For ^{8}B, there are significant amount of the PLF component as the primary fragment, but very few remain without particle decay. Figures 11 and 12 shows that these primary ^{8}B fragments were formed with low excitation energies peaked near $E_x = 0$ just in a way similar to other light nuclei, most probably due to the intercluster correlations. However, the method does not produce fragments exactly in the ground state. A slight spurious excitation is not usually a problem as far as the state is treated as stable in the secondary decay code. Unlike most of the light nuclei, the ^{8}B nucleus is affected by this subtle problem because of its very low particle decay threshold. Its first excited state at 0.77 MeV is already unstable for proton emission. In such a case, it would be more reasonable to regard the low excitation component as the ground state without processing it with the secondary decay. A more fundamental argument can be given based on the wave function $|\Phi_{\mathrm{frag}}\rangle$

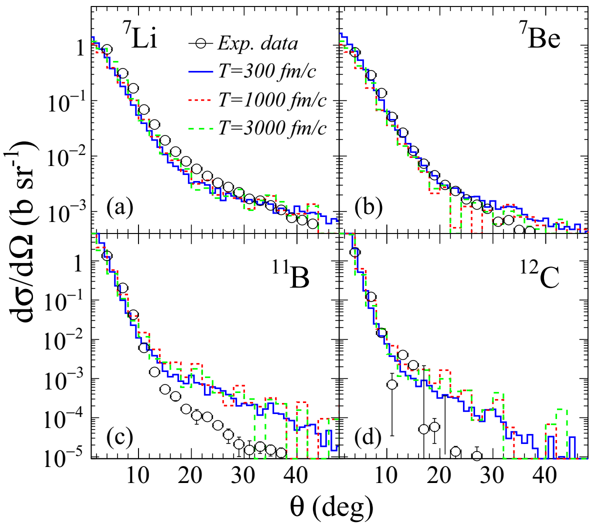

FIG. 14. Comparisons of angular distributions of typical isotopes in different switching times from AMD to GEMINI for selected IMFs, ^{7}Li, ^{7}Be, ^{11}B, and ^{12}C in (a)–(d), respectively. The experimental data are shown by solid circles. The calculated results of the different switching time at 300, 1000, and 3000 fm/c are shown by blue solid, red dotted, and green dashed histograms, respectively. No forced-decay is used. See details in the text.

of the internal state of each primary fragment. As mentioned above, the energy expectation value $\langle \Phi_{\text{frag}}|H|\Phi_{\text{frag}}\rangle$ is used in the standard prescription to obtain the excitation energy E_{x}. However, the state $|\Phi_{\text{frag}}\rangle$ is a superposition of many energy eigenstates in general, and therefore a more reasonable way is to choose a nuclear level $|\Psi_i\rangle$ randomly based on the overlap probability $|\langle \Psi_i|\Phi_{\text{frag}}\rangle|^2$. Even if the energy expectation value is above the particle decay threshold, the state can have a significant overlap probabilities with stable states. This would automatically solve the issue for ^{6}Li mentioned above. The same argument may be applied to the primary heavy PLFs, which seem to be decaying too much. However, such a treatment is not within the scope of this paper.

The production of ^{8}B by a neutron emission of ^{9}B may be rare because it is possible only at high excitation energies of ^{9}B above 18.6 MeV while there are other decay channels already open below this energy. In fact, feeding of ^{8}B from ^{9}B is suppressed significantly in the AMD+GEMINI simulation. Since the yield of the primary PLF of ^{9}B is more than ten times larger than that of ^{8}B, if 5–10 % of them decayed by a neutron decay, it would be sufficient for the observed PLF yields of ^{8}B.

E. Switching time from AMD to GEMINI

The switching time from the AMD calculations to GEMINI, the afterburner may change the yields distributions if the dynamical breakup is still important after the switching time. The results of the different switching times for typical isotopes, ^{7}Li, ^{7}Be, ^{11}B, and ^{12}C, are compared in Fig. 14 between the switching time at 300 fm/c, which is shown in Figs. 1 and 3, those at $t = 1000$ fm/c and $t = 3000$ fm/c. The results are taken from the GEMINI output and no forced-decay program is used for the calculation. As shown in the figure, the observed differences are very small, indicating that the decay of the excited fragments after $t = 300$ fm/c are dominated by a statistical decay process, which is treated by the afterburner GEMINI in the present work.

V. SUMMARY

The angular distributions and energy spectra of all experimentally observed ejectiles from the ^{12}C + ^{12}C reaction at 95 MeV/nucleon of Ref. [1] are studied, compared to those of a modified version of AMD, where cluster correlations are taken into account in the final states of the two-nucleon collision process to form light clusters with $A \leqslant 4$. Correlations between clusters are also taken into account to form light nuclei by binding several light clusters. This extended version of AMD reproduces the global characteristic of the LCP and IMF emissions to some extent. In particular, not only light clusters but also many of light nuclei with $A \leqslant 9$ are emitted with very low excitation energies in the IV component in violent events. However, in detail, there are some problems. For LCPs, the calculation underestimates the production, except that α particles are rather well reproduced in their angular distribution and energy spectra. We have found that it is important to carefully handle the excitation energies of primary fragments and their statistical decays. The AMD+GEMINI calculation reproduces the production of IMFs with $A = 7$ very well but significantly underpredicts the yields of ^{6}Li and ^{8}B at all angles and overpredicts the yields of isotopes with $9 \leqslant A \leqslant 12$ at $\theta_{\text{lab}} > 20^\circ$. The possible reasons for these discrepancies are discussed with the method to extract the excitation energy from the wave function of each primary fragment and with the large survivability of IMFs with the excitation energy above the particle decay threshold in the GEMINI calculation. However, overall the calculated results of AMD with cluster correlations indicate that the cluster correlations have strong impacts on the emissions of IV component of IMFs.

The cluster correlations in the present model can be too strong in principle because the correlations are introduced as much as possible, while the properties of clusters may be modified in medium. It is an interesting future subject to study the relation between the strength of cluster correlations and the particle composition of the IV source component.

ACKNOWLEDGMENTS

We thank to R. J. Charity for a useful comment about the Gemini simulation. This work is supported by the National Natural Science Foundation of China (Grants No. 11605257 and No. 91426301), and CAS "Light of West China" Program (Grant No. 29Y725030). This work is also supported by the US Department of Energy under Grant No. DE–FG02–93ER40773. A.O. acknowledges support from Japan Society for the Promotion of Science KAKENHI Grants No. 24105008 and No. 17K05432.

[1] J. Dudouet, D. Juliani, M. Labalme, D. Cussol, J. C. Angélique, B. Braunn, J. Colin, Ch. Finck, J. M. Fontbonne, H. Guérin, P. Henriquet, J. Krimmer, M. Rousseau, M. G. Saint-Laurent, and S. Salvador, Phys. Rev. C **88**, 024606 (2013); http://hadrontherapy-data.in2p3.fr.

[2] J. Dudouet, D. Cussol, D. Durand, and M. Labalme, Phys. Rev. C **89**, 054616 (2014).

[3] J. Dudouet and D. Durand, Phys. Rev. C **94**, 014616 (2016).

[4] G. Tian, R. Wada, Z. Chen *et al.*, Phys. Rev. C **95**, 044613 (2017).

[5] W. Lin, X. Liu, R. Wada, M. Huang, P. Ren, G. Tian, F. Luo, Q. Sun, Z. Chen, G. Q. Xiao, R. Han, F. Shi, J. Liu, and B. Gou, Phys. Rev. C **94**, 064609 (2016).

[6] A. Ono, H. Horiuchi, T. Maruyama, and A. Ohnishi, Prog. Theor. Phys. **87**, 1185 (1992).

[7] A. Ono, Phys. Rev. C **66**, 014603 (2002).

[8] A. Ono and H. Horiuchi, Prog. Part. Nucl. Phys. **53**, 501 (2004).

[9] L. Chen *et al.*, Nucl. Phys. A **729**, 809 (2003).

[10] D. D. S. Coupland, W. G. Lynch, M. B. Tsang, P. Danielewicz, and Y. Zhang, Phys. Rev. C **84**, 054603 (2011).

[11] A. Ono, J. Phys.: Conf. Ser. **420**, 012103 (2013).

[12] N. Ikeno, A. Ono, Y. Nara, and A. Ohnishi, Phys. Rev. C **93**, 044612 (2016).

[13] A. Ono, Il Nuovo Cimento C **39**, 390 (2016).

[14] Y. Kanada-En'yo, H. Horiuchi, and A. Ono, Phys. Rev. C **52**, 628 (1995).

[15] A. Ono, H. Horiuchi, and T. Maruyama, Phys. Rev. C **48**, 2946 (1993).

[16] A. Ono, H. Horiuchi, Toshiki Maruyama, and A. Ohnishi, Phys. Rev. Lett. **68**, 2898 (1992).

[17] E. Chabanat *et al.*, Nucl. Phys. A **635**, 231 (1998); **643**, 441(E) (1998).

[18] A. Ono and H. Horiuchi, Phys. Rev. C **53**, 2958 (1996).

[19] G. Röpke, Nucl. Phys. A **867**, 66 (2011).

[20] P. Danielewicz and G. F. Bertsch, Nucl. Phys. A **533**, 712 (1991).

[21] A. Ono, Phys. Rev. C **59**, 853 (1999).

[22] R. J. Charity, Phys. Rev. C **82**, 014610 (2010).

[23] R. Wada, K. Hagel, J. Cibor, M. Gonin, T. Keutgen, M. Murray, J. B. Natowitz, A. Ono, J. C. Steckmeyer, A. Kerambrum, J. C. Angélique, A. Auger, G. Bizard, R. Brou, C. Cabot, E. Crema, D. Cussol, D. Durand, Y. El Masri, P. Eudes, Z. Y. He, S. C. Jeong, C. Lebrun, J. P. Patry, A. Péghaire, J. Peter, R. Régimbart, E. Rosato, F. Saint-Laurent, B. Tamain, and E. Vient, Phys. Rev. C **62**, 034601 (2000).

[24] R. Wada, T. Keutgen, K. Hagel, Y. G. Ma, J. Wang, M. Murray, L. Qin, P. Smith, J. B. Natowitz, R. Alfarro, J. Cibor, M. Cinausero, Y. El Masri, D. Fabris, E. Fioretto, A. Keksis, S. Kowalski, M. Lunardon, A. Makeev, N. Marie, E. Martin, Z. Majka, A. Martinez-Davalos, A. Menchaca-Rocha, G. Nebbia, G. Prete, V. Rizzi, A. Ruangma, D. V. Shetty, G. Souliotis, P. Staszel, M. Veselsky, G. Viesti, E. M. Winchester, S. J. Yennello, W. Zipper, and A. Ono, Phys. Rev. C **69**, 044610 (2004).

[25] J. C. Steckmeyer, A. Kerambrun, J. C. Angélique, G. Auger, G. Bizard, R. Brou, C. Cabot, E. Crema, D. Cussol, D. Durand, Y. El Masri, P. Eudes, M. Gonin, K. Hagel, Z. Y. He, S. C. Jeong, C. Lebrun, J. P. Patry, A. Péghaire, J. Péter, R. Régimbart, E. Rosato, F. Saint-Laurent, B. Tamain, E. Vient, and R. Wada, Phys. Rev. Lett. **76**, 4895 (1996).

[26] R. J. Charity (private communication).